

## Convective Dynamo Simulation with a Grand Minimum

Kyle Augustson<sup>1</sup> with Sacha Brun<sup>2</sup>, Mark Miesch<sup>1</sup>, and Juri Toomre<sup>3</sup>

<sup>1</sup>*High Altitude Observatory, 3080 Center Green Drive, Boulder, Colorado USA 80301*

<sup>2</sup>*Laboratoire AIM Paris-Saclay, CEA/Irfu Université Paris-Diderot CNRS/INSU, 91191 Gif-sur-Yvette*

<sup>3</sup>*JILA, University of Colorado, Boulder, Colorado USA 80309*

**Abstract.** The global-scale dynamo action achieved in a simulation of a Sun-like star rotating at thrice the solar rate is assessed. The 3-D MHD Anelastic Spherical Harmonic (ASH) code, augmented with a viscosity minimization scheme, is employed to capture convection and dynamo processes in this G-type star. The simulation is carried out in a spherical shell that encompasses 3.8 density scale heights of the solar convection zone. It is found that dynamo action with a high degree of time variation occurs, with many periodic polarity reversals occurring roughly every 6.2 years. The magnetic energy also rises and falls with a regular period. The magnetic energy cycles arise from a Lorentz-force feedback on the differential rotation, whereas the processes leading to polarity reversals are more complex, appearing to arise from the interaction of convection with the mean toroidal fields. Moreover, an equatorial migration of toroidal field is found, which is linked to the changing differential rotation, and potentially to a nonlinear dynamo wave. This simulation also enters a grand minimum lasting roughly 20 years, after which the dynamo recovers its regular polarity cycles.

### 1. Introduction

The Sun exhibits many time scales from the ten minute lifetimes of granules to multi-millennial magnetic activity modulations. One of the most prominent of these scales is the roughly 11-year sunspot cycle, during which the number of magnetically active regions waxes and wanes. Observations of the magnetic field at the solar surface reveal complex, hierarchical structures existing on a vast range of spatial scales. Despite these complexities, large-scale organized spatial patterns such as Maunder's butterfly diagram, Joy's law, and Hale's polarity law suggest the existence of a structured large-scale magnetic field within the solar convection zone. In particular, on the Sun's surface active regions initially emerge at mid-latitudes and appear at increasingly lower latitudes as the cycle progresses, thus exhibiting equatorward migration (e.g., Hathaway, 2010).

Such large-scale magnetic phenomenon that vary with the solar cycle are likely being sustained through convective dynamo action occurring within the solar interior. It has been suspected for at least 60 years that the crucial ingredients for the solar dynamo are the shear of the differential rotation and the helical

nature of the small-scale convective flows present in the solar convection zone (e.g., Parker, 1955; Steenbeck & Krause, 1969; Parker, 1977). Yet even with the advancement to fully nonlinear global-scale 3-D MHD simulations (e.g., Gilman, 1983; Glatzmaier, 1985; Brun et al., 2004; Browning et al., 2006), achieving dynamo action that exhibits the basic properties of Sun’s magnetism has been quite challenging. Nonetheless, recent global-scale simulations of convective dynamos have begun to make substantial contact with some of the properties of the solar dynamo through a wide variety of numerical methods (e.g., Brown et al., 2011; Racine et al., 2011; Käpylä et al., 2012; Nelson et al., 2013).

## 2. Computational Methods

The simulation of convection and dynamo action presented here uses the ASH code to evolve the anelastic equations for a conductive calorically perfect gas in a rotating spherical shell. ASH solves these equations with a spherical harmonic decomposition of the entropy, magnetic field, pressure, and mass flux in the horizontal directions. Either a Chebyshev polynomial representation (Clune et al., 1999; Miesch et al., 2000), or a fourth order non-uniform finite difference in the radial direction, resolve radial derivatives. The radial finite difference derivative scheme is used here. The solenoidality of the mass flux and magnetic vector fields is maintained through the use of a stream function formalism (Brun et al., 2004). The Crank-Nicholson implicit time-stepping method advances the linear terms in the MHD equations including eddy diffusion, pressure gradients, and buoyancy. Nonlinear terms such as the convective derivatives, Lorentz forces, and dissipative processes are handled with a second-order Adams-Bashforth time step. The boundary conditions used are impenetrable on radial boundaries, with a constant radial gradient of the specific entropy there as well. The magnetic boundary conditions are perfectly conducting at the lower boundary and extrapolated as a potential field at the upper boundary. Furthermore, the latest version of the ASH code is employed, where the necessary MPI communication pathways and memory layout have been overhauled.

A slope-limited diffusion (SLD) mechanism similar to the scheme presented in Rempel et al. (2009) and Fan et al. (2013) was implemented into the reformulated ASH code. The SLD acts locally to achieve a spatially monotonic solution by limiting the linearly reconstructed slope in each coordinate direction. The scheme minimizes the steepest gradients through the action of the minmod limiter, while the rate of diffusion is regulated by the local velocity. The rate of diffusion is further reduced through a function  $\phi$  of the ratio of the cell-edge difference  $\delta q_i$  and the cell-center difference  $\Delta q_i$  in a given direction  $i$  for the quantity  $q$ . Similar to Rempel et al. (2009), this function is defined as  $\phi_i = (\text{minmod}[\delta q_i, \Delta q_i])^8$ . This function limits the action of the diffusion to regions with large differences in the reconstructed solutions at cell-edges. Since SLD is a nonlinear operator, it is computed in physical space, incurring the cost of smaller time steps due to the convergence of the grid at the poles. The resulting diffusion fields are projected back into spectral space and added to the solution through the Adams-Bashforth scheme used for the other nonlinear terms.

The simulation encompasses the bulk of the solar convection zone and the full spherical geometry, though the rotation rate of the frame is  $\Omega_0 = 3\Omega_\odot$ . The domain stretches from the base of the convection zone at  $0.715 R_\odot$  to  $0.965 R_\odot$ ,

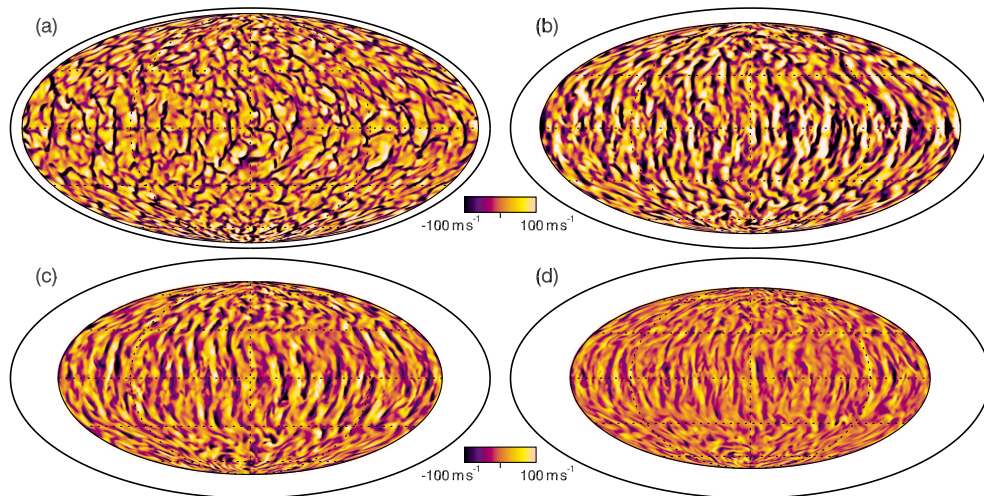


Figure 1: *Snapshots of the horizontal convective patterns arising in the radial velocity  $v_r$  from the ASH simulation presented here that uses slope-limited diffusion are shown in Mollweide projection and sampled at four depths: (a)  $0.95 R_\odot$ , (b)  $0.87 R_\odot$ , (c)  $0.80 R_\odot$ , (d)  $0.75 R_\odot$ . The patterns possess larger-scale columnar convection at low latitudes and the smaller-scales at higher latitudes, with downflows dark and upflows in lighter tones. The velocity range is the same for each panel, as indicated with the colorbar.*

omitting the tachocline and the deep radiative interior as well as the complex physics of the near-surface layers and approximating their action with an impenetrable boundary. The SLD has been restricted to act only on the velocity field in this simulation. This mimics a lower thermal and magnetic Prandtl number ( $Pr$ ,  $Pm$ ) than otherwise obtainable through an elliptic diffusion operator. Yet the entropy and magnetic fields remain under the influence of an inhomogeneous eddy diffusion, with a radially dependent entropy diffusion coefficient  $\kappa_S$  and magnetic diffusivity  $\eta$ . The magnitude and form of these two diffusion coefficients are similar to those of case D3 from Brown et al. (2010), with  $\kappa_S, \eta \propto \bar{\rho}^{-1/2}$ , with  $\bar{\rho}$  the spherically symmetric density. However, this case has about twice the density contrast across the domain, being 45 rather than 26, and has a resolution of  $N_r \times N_\theta \times N_\phi = 200 \times 256 \times 512$ . In keeping with the ASH nomenclature for the simulations explored in Brown et al. (2010), Brown et al. (2011), and Nelson et al. (2013), this dynamo solution has been called K3S.

### 3. Global-Scale Convective Dynamo Action

Global-scale convective dynamo simulations in rotating spherical shells have recently achieved the long-sought goal of cyclic magnetic polarity reversals with a multi-decadal period. Moreover, some of these simulations have illustrated that large-scale dynamo action is possible within the bulk of the convection zone, even in the absence of a tachocline (Brown et al., 2010). Global-scale MHD simulations of a more rapidly rotating Sun with the pseudo-spectral ASH code have produced polarity reversing dynamo action that possesses strong toroidal wreaths of mag-

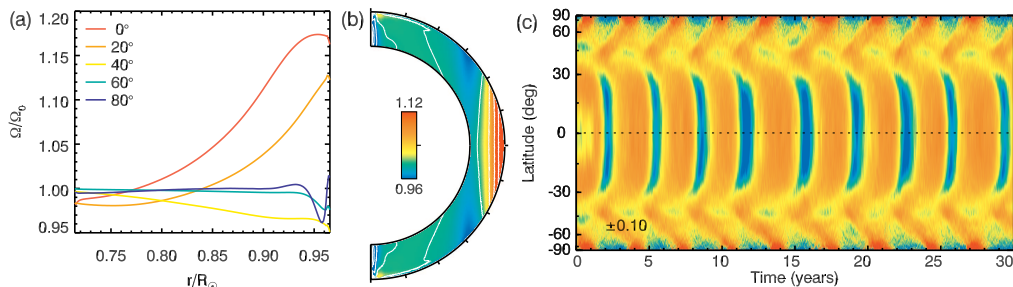


Figure 2.: *The properties of the differential rotation in K3S. (a) Cuts at constant latitude through the time-averaged, azimuthally-averaged, and normalized angular velocity  $\langle\langle\Omega\rangle\rangle/\Omega_0$  (double brackets indicating dual averages and  $\Omega_0$  the frame rotation rate of  $3\Omega_\odot$ ), showing a fast equator and slow poles. (b)  $\langle\langle\Omega\rangle\rangle/\Omega_0$  shown in the meridional plane, illustrating the nearly cylindrical rotation profile. (c) A time-latitude diagram of azimuthally-averaged  $\langle\Delta\Omega\rangle = \langle\Omega\rangle - \langle\langle\Omega\rangle\rangle$  in cylindrical projection, elucidating the propagation of equatorial and polar branches of a torsional oscillation arising from strong Lorentz-force feedback. The color indicates enhanced differential rotation in red and periods of slower rotation in blue, with variations of up to  $\pm 10\%$  of the bulk rotation rate.*

netism that propagate poleward as a cycle progresses (Brown et al., 2011; Nelson et al., 2013), much like the earlier work of Gilman (1983) and Glatzmaier (1985). These fields are seated within the convection zone, with much of the magnetic energy being near the base of the convection zone. The perfectly conducting lower boundary condition used here and in those simulations requires the field to be horizontal there, which tends to promote the formation of longitudinal structure in the presence of a differential rotation.

Contemporaneously, implicit large-eddy simulations (ILES) have paved the road toward more orderly long-term cycles in a setting that mimics the solar interior. Indeed, simulations utilizing the Eulerian-Lagrangian (EULAG) code produce regular polarity cycles occurring roughly every 80 years in the presence of a tachocline and with the bulk of the magnetic field existing at higher latitudes (Ghizaru et al., 2010). This simulation showed radial propagation of structures but little latitudinal variation during a cycle. More recent simulations of a Sun-like star rotating at  $3\Omega_\odot$  also produce low-latitude poleward propagating solutions (Charbonneau, 2013). In both cases, such dynamo action is accomplished through two mechanisms: first by reducing the enthalpy transport of the largest scales through a simple sub-grid-scale (SGS) model that diminishes thermal perturbations over a roughly 1.5 year time scale, serving to moderate the global Rossby number; and second through the ILES formulation of the semi-implicit EULAG MHD code that attempts to maximize the complexity of the flows and magnetic fields for a given spatial resolution.

Inspired by these recent ASH and EULAG results, an attempt has been made to make contact with both numerical methods through the incorporation of SLD into ASH with the express goal of achieving a low effective Pr and Pm dynamo. Thus an attempt is made to better mimic the low Prandtl number solar setting, while keeping the eddy-diffusive approximation for entropy mixing and treating the reconnection of small-scale magnetic field as diffusive. This effort minimizes

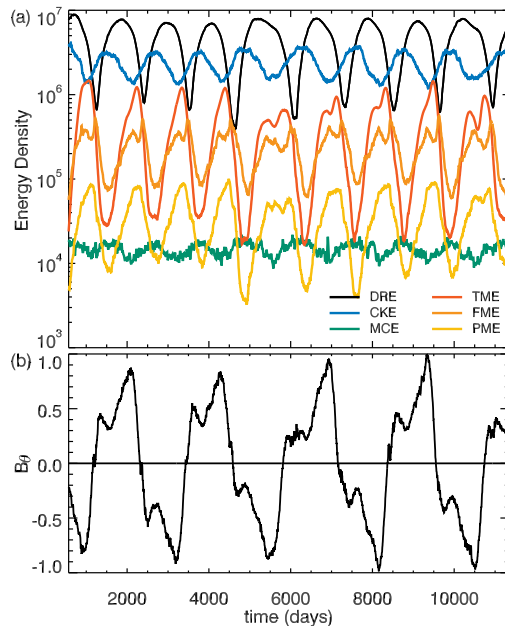


Figure 3.: *Volume-averaged energy densities and latitudinal magnetic field in K3S. (a) Time traces of volume-averaged energy densities associated with the differential rotation (DRE), turbulent convective kinetic energy (CKE), meridional circulation (MCE), toroidal magnetic field (TME), fluctuating magnetic field (FME), and the poloidal magnetic field (PME). The magnetic energy cycle is evident. (b) The horizontally-averaged and normalized latitudinal magnetic field ( $B_\theta$ ) shown at mid-convection zone, illustrating the magnetic polarity cycle.*

the effects of viscosity, and so extends the inertial range as far as possible for a given resolution. Thus SLD permits more scales to be captured before entering the dissipation range. With this newly implemented diffusion minimization scheme, a solution was obtained that possesses four fundamental features of the solar dynamo: a regular magnetic energy cycle period, and an orderly magnetic polarity cycle with a period of  $\tau_C = 6.2$  years, equatorward propagation of magnetic features, and poleward migration of oppositely signed flux. Furthermore this equilibrium is punctuated by an interval of relative quiescence, after which the cycle is recovered.

#### 4. Convective Dynamics in K3S

Some aspects of the nature of the convective dynamics achieved within K3S are visible in Figure 1. In the upper convection zone, the downflows are roughly twice as fast as the upflows, with the rms upflow being about  $100 \text{ m s}^{-1}$  and the downflow roughly  $-200 \text{ m s}^{-1}$ . This decreases with depth, with the asymmetry between the up and downflows nearly vanishing, with the typical velocity being about  $10 \text{ m s}^{-1}$ . The convection is very columnar reflecting the strength of the Coriolis force acting upon it, which tends to tilt the convective structures toward the rotation axis. In particular, when viewed at a constant radius, the convective

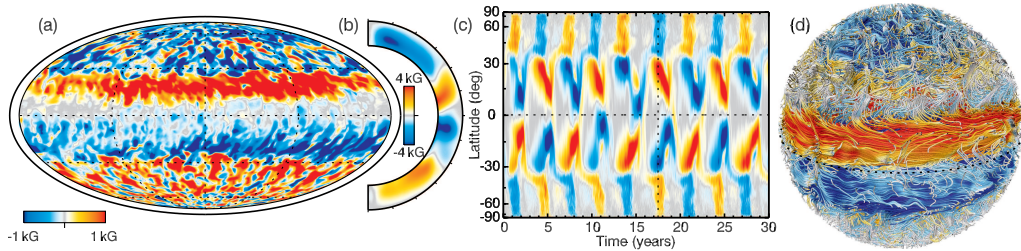


Figure 4.: *Nature of the toroidal magnetic field  $B_\phi$ . (a) Snapshot of the horizontal structure of  $B_\phi$  at  $0.95 R_\odot$  shown in Mollweide projection, at the time corresponding to the vertical dashed line in (c). This illustrates the azimuthal connectivity of the magnetic wreaths, with the polarity of the field such that red (blue) tones indicate positive (negative) toroidal field. (b) Azimuthally-averaged  $\langle B_\phi \rangle$  also time-averaged over a single energy cycle, depicting the structure of the toroidal field in the meridional plane. (c) Time-latitude diagram of  $\langle B_\phi \rangle$  at  $0.95 R_\odot$  in cylindrical projection, exhibiting the equatorward migration of the wreaths from the tangent cylinder at roughly  $38^\circ$  and the poleward propagation of the higher latitude field. The color and scaling is as in (a). (d) A rendering of magnetic field lines in the domain colored by the magnitude and sign of  $B_\phi$ , with strong positively oriented field in red, and the strong oppositely directed field in blue.*

structures appear as elongated and north-south aligned flows at low latitudes and smaller scales at higher latitudes (see Figure 1). In aggregate, the spatial structure and flow directions along these cells produce strong Reynolds stresses that act to accelerate the equator and slow the poles. The Reynolds stresses arising from these turbulent structures are the dominant mechanism that maintains the differential rotation, as the viscous stresses are quite small in this simulation. The collective action of these cells also leads to a significant latitudinal enthalpy flux that heats the poles and sustains the thermal wind balance between the differential rotation and the latitudinal entropy gradient. The thermal wind in concert with the Reynolds stresses serves to rebuild and maintain the differential rotation during each cycle. Indeed, a substantial differential rotation is established and maintained here, as can be seen in Figure 2. It is also apparent at higher latitudes and just below the upper boundary that this simulation has a negative radial gradient in the angular velocity  $\Omega$  (Figure 2a), akin to the near-surface shear layer that is well-known from helioseismology. The reason for its formation is likely a numerical boundary layer effect rather than capturing the physical processes present in the solar near-surface shear layer. However, the Maxwell stresses are certainly important during the latter phases of a magnetic energy cycle where they act to quench both the convection and the differential rotation, which is evident in the volume averaged energy traces of Figure 3.

The variable nature of the convective patterns over a cycle is an important piece of the K3S dynamo. Indeed, the magnetic fields disrupt the alignment and correlations of these cells through Lorentz forces. Particularly, as the field gathers strength during a cycle, the strong azimuthally-connected toroidal fields tend to create a thermal shadow that weakens the thermal driving of the equatorial cells. Thus their angular momentum transport is also diminished, which explains why the differential rotation seen in Figure 2(b) cannot be fully maintained during



the cycle. This is captured in the modulation of the kinetic energy contained in the fluctuating velocity field, which here varies by about 50% throughout the cycle as is visible in Figure 3(a). Such a mechanism is in keeping with the impacts of strong toroidal fields in the convection zone suggested by Parker (1987). Moreover, strong nonlinear Lorentz force feedbacks have been seen in other convective dynamo simulations as well (Brown et al., 2011), and they have been theoretically realized for quite some time (Malkus & Proctor, 1975).

Figure 4 illustrates the morphology of the toroidal fields in space and time. The presence of large-scale and azimuthally-connected structures is evident in Figures 4(a, d). Such toroidal structures have been dubbed wreaths (Brown et al., 2010). In K3S, there are two counter-polarized, lower-latitude wreaths that form near the point where the tangent cylinder intersects horizontal surfaces. This site is also where the peak in the latitudinal gradient of the differential rotation exists for much of a magnetic energy cycle. There are also polar caps of magnetism of the opposite sense to those at lower latitudes. These caps serve to moderate the polar differential rotation, which would otherwise tend to accelerate and hence establish fast polar vortices. The average structure of the wreaths and caps is apparent in Figure 4(b), which is averaged over a single energy cycle (3.1 years). The wreaths appear rooted at the base of the convection zone, whereas the caps have the bulk of their energy in the lower convection zone above its base. This is somewhat deceptive as the wreaths are initially generated higher in the convection zone, while the wreath generation mechanism (primarily the  $\Omega$ -effect) migrates equatorward and toward the base of the convection zone over the course of the cycle. The wreaths obtain their greatest amplitude at the base of the convection zone and thus appear seated there.

## 5. Grand Minima and Long-Term Modulation

As with some other dynamo simulations (e.g., Brown et al., 2011; Augustson et al., 2013), there is also a degree of long-term modulation of the magnetic cycles in case K3S. Figure 5 shows an interval of about 20 years during which the polarity cycles are lost, though the magnetic energy cycles resulting from the nonlinear interaction of the differential rotation and the Lorentz force remain. During this interval, the magnetic energy in the domain is about 25% lower, whereas the energy in the volume encompassed by the lower-latitudes is decreased by 60%. However, both the spatial and temporal coherency of the cycles are recovered after this interval and persist for the last 40 years of the 100 year-long simulation. Prior to entering this quiescent period, there was an atypical cycle with only the northern hemisphere exhibiting equatorward propagation. This cycle also exhibits a prominent loss of the equatorial anti-symmetry in its magnetic polarity. The subsequent four energy cycles do not reverse their polarity, which is especially evident in the polar regions, whereas the lower latitudes do seem to attempt such reversals.

Similar quasi-periodic dynamo action has been previously reported on, though only in mean-field models and in reduced dynamo models and not in fully nonlinear 3D MHD simulations. Some of the most well-studied quasi-periodic systems utilize reduced dynamo models that couple only a few modes of the overall system, such as those models of Weiss et al. (1984). Weiss uses a simple  $\alpha\Omega$  dynamo model. This is accomplished through systems of coupled nonlinear ordi-

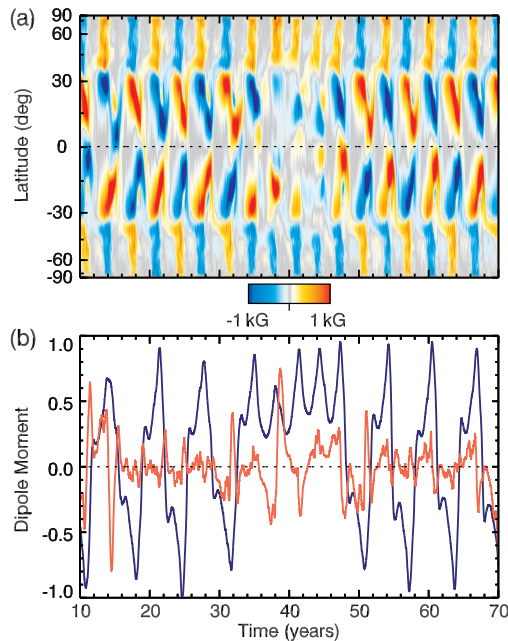


Figure 5.: *An interval of magnetic quiescence. (a) Time-latitude diagram of  $\langle B_\phi \rangle$  at  $0.95 R_\odot$  in cylindrical projection, picturing the loss and reappearance of cyclic polarity reversals as well as the lower amplitude of the wreaths. Strong positive toroidal field is shown as red, negative in blue. (b) Normalized magnetic dipole moment (blue) and quadrupole moment normalized by the dipole absolute maximum (red). There is a significant rise in the quadrupole moment near reversals, suggesting a brief coupling between families of dipolar and quadrupolar dynamo modes.*

nary differential equations, where the number of included modes is varied. This results in models that range from fourth to sixth-order in their time derivative. These models admit simple nonlinear oscillatory solutions. The highest-order model with the largest number of dynamic modes exhibits transitions from periodic oscillations to chaotic behavior with longer-term modulation akin to the grand minima in the solar activity cycle.

Later work explored alternative dynamo feedback mechanisms in these low-order systems (Tobias, 1997). Tobias explored the impacts that modulations in the toroidal magnetic field energy and that Lorentz-force feedback on the large-scale flows have on the character and evolution of nonlinear  $\alpha\Omega$  dynamo solutions. The former mechanism is shown to affect the parity of the dynamo, whereas the latter can reduce the efficiency of both the  $\alpha$  and  $\Omega$  effects in the limit of low magnetic Prandtl numbers. With an appropriate choice of parameters, some solutions exhibit a long-term evolution that produces grand extrema, while retaining the basic cycle periods, as the Sun is observed to do. In particular, it is shown that the magnetic field can be substantially modulated and effectively remain dipolar. During grand minima the magnetic field is weak and is no longer a simple dipole. Such behavior is also seen in the simulation here, where its grand minimum is associated with a much stronger quadrupole moment, as is evident in Figure 5b. It also worth noting that the quadrupole component tends



to briefly spike during the polarity reversal, which may be a signal of the reversal mechanism. Indeed, recent work has explored solar observations over the past three solar cycles to assess the magnetic energy contained in a large range of spherical harmonic modes (DeRosa et al., 2012). It is seen there that the coupling between the dipolar and quadrupolar families of modes correlates well with the large-scale polarity reversals of the Sun. Similar phenomenon seen in the K3S simulation will be explored further in a forthcoming paper.

## 6. Generating Global-Scale Magnetism

The toroidal field shown in Figure 4 is initially generated and then maintained by similar processes. During the growth phase of the magnetic field, the shear of the differential rotation acts to fold and wind the initial poloidal field into toroidal structures. During this kinematic phase, the mean shear and meridional flows are largely unaffected and can be considered stationary relative to the time scales of the growing field. However, once the magnetic fields are strong enough they begin to quench the convective flows that cross them. The magnetic field strength becomes saturated as the back reaction of the Lorentz forces increases the alignment of the velocity field and the magnetic field, which reduces both its generation and at times leads to its partial destruction.

This configuration of fields establishes a new balance between the various mechanisms of angular momentum transport needed to sustain the differential rotation when compared to a hydrodynamic simulation. Here magnetic fields both transport angular momentum as well as block formerly open channels of transport. For instance, the strong toroidal field serves to reduce the latitudinal transport of angular momentum by Reynolds stresses, which modifies both the differential rotation and the meridional circulations within the simulation relative to what would be achieved in a hydrodynamic simulation.

Since the dynamo running within K3S waxes and wanes as time marches forward through many polarity reversals, the balance between magnetic field generation mechanisms is not instantaneous nor is it the same at any given time within the cycle. When averaged in time over the full span of the simulation, though neglecting the interval of the grand minimum, an analysis of the terms contributing to the generation and destruction of magnetic energy can illustrate those mechanisms that have the greatest overall influence on the dynamo. The evolving magnetic fields arise from many competing processes that both produce and destroy magnetic field. These processes are: the shearing and advection of field, compressive motions, and dissipation through resistive processes. These production and dissipation terms are most easily understood by an evolution equation for the magnetic energy contained in the mean magnetic fields. This equation can be broken into its poloidal and toroidal components  $P_{ME}$  and  $T_{ME}$  as

$$\begin{aligned} \frac{\partial T_{ME}}{\partial t} = \frac{\langle B_\phi \rangle}{8\pi} & \left[ \overbrace{\langle (\mathbf{B}) \cdot \nabla \rangle \langle \mathbf{v} \rangle}_T \Big|_\phi + \overbrace{\langle (\mathbf{B}' \cdot \nabla) \mathbf{v}' \rangle}_T \Big|_\phi - \overbrace{\langle (\mathbf{v}) \cdot \nabla \rangle \langle \mathbf{B} \rangle}_T \Big|_\phi \right. \\ & \left. - \overbrace{\langle (\mathbf{v}' \cdot \nabla) \mathbf{B}' \rangle}_T \Big|_\phi + \overbrace{\langle B_\phi v_r \rangle}_{T_{CC}} \frac{\partial \ln \bar{\rho}}{\partial r} - \overbrace{\nabla \times (\eta \nabla \times \langle \mathbf{B} \rangle)}_T \Big|_\phi \right], \end{aligned} \quad (1)$$

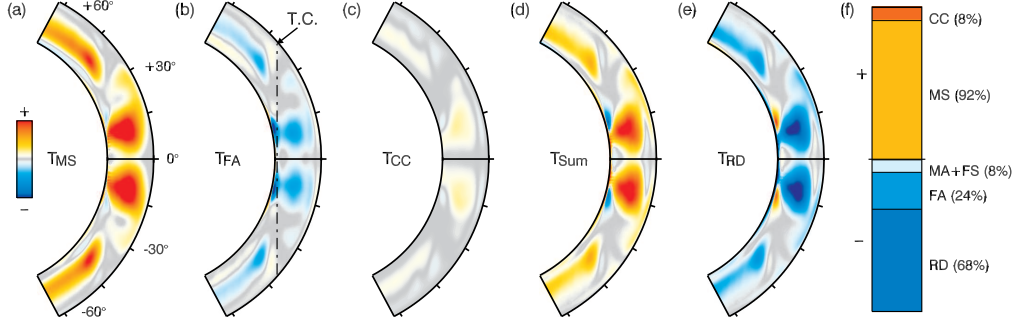


Figure 6.: Generation of mean toroidal magnetic energy ( $T_{ME}$ ) in *K3S*. The view is from  $\pm 60^\circ$  to emphasize the equatorial regions. Here only the dominant production terms are shown, namely (a) mean shear ( $T_{MS}$ ), (b) fluctuating advection ( $T_{FA}$ ), with a cylinder tangent to the bottom of the domain (*T.C.*) is indicated (dashed line), (c) compressive correlations ( $T_{CC}$ ), (d) the sum  $T_{MS} + T_{FS} + T_{MA} + T_{FA} + T_{CC}$ , which largely act in concert to balance (e) the resistive diffusion of field ( $T_{RD}$ ). All panels have identical scaling. The mean generation terms shown here contribute to the  $T_{ME}$  when positive (red), and destroy it if they are negative (blue). (f) The relative contribution of each term, with terms in red toned regions adding to the volume and time-averaged toroidal energy generation and those in blue dissipating energy.

$$\frac{\partial P_{ME}}{\partial t} = \frac{\langle \mathbf{B}_P \rangle}{8\pi} \cdot \left[ \overbrace{\langle (\langle \mathbf{B} \rangle \cdot \nabla) \langle \mathbf{v} \rangle \rangle}^{P_{MS}} + \overbrace{\langle (\mathbf{B}' \cdot \nabla) \mathbf{v}' \rangle}^{P_{FS}} - \overbrace{\langle (\langle \mathbf{v} \rangle \cdot \nabla) \langle \mathbf{B} \rangle \rangle}^{P_{MA}} - \overbrace{\langle (\mathbf{v}' \cdot \nabla) \mathbf{B}' \rangle}^{P_{FA}} \right. \\ \left. + \overbrace{\langle \mathbf{B}_{PVr} \rangle \frac{\partial \ln \bar{\rho}}{\partial r}}^{P_{CC}} - \overbrace{\nabla \times (\eta \nabla \times \langle \mathbf{B} \rangle)}^{P_{RD}} \right], \quad (2)$$

with the  $\langle \rangle$  denoting an average in longitude,  $\mathbf{v}' = \mathbf{v} - \langle \mathbf{v} \rangle$  the fluctuating velocity,  $\mathbf{B}' = \mathbf{B} - \langle \mathbf{B} \rangle$  the fluctuating magnetic field, and  $\langle \mathbf{v} \rangle$  and  $\langle \mathbf{B} \rangle$  the axisymmetric velocity and magnetic field respectively. A detailed derivation of the mean-field production terms in spherical coordinates is provided in Appendix A of Brown et al. (2010). Here  $T$  indicates a toroidal magnetic energy generation term and  $P$  a poloidal energy generation term. The subscripts denote production in turn by mean shear (MS), fluctuating shear (FS), mean advection (MA), fluctuating advection (FA), compressional correlations (CC), and resistive diffusion (RD).

Over a long time average, the time variability of the production of  $T_{ME}$  is removed, leaving a balance between terms that produce and terms that destroy field. Figure 6 presents such a time average of these mean generation terms, involving the entire evolution of case *K3S* over an 80 year interval (3300 rotations). In this statistically steady state, the maintenance of the toroidal wreaths of magnetic field is largely governed by a balance between the production of field by both the mean shear and the dissipation of field through resistive processes. By comparing Figures 6(a) and 6(d), it is clear that the mean shear  $T_{MS}$  of Equation (1) is primarily responsible for maintaining the strength of the wreaths. The

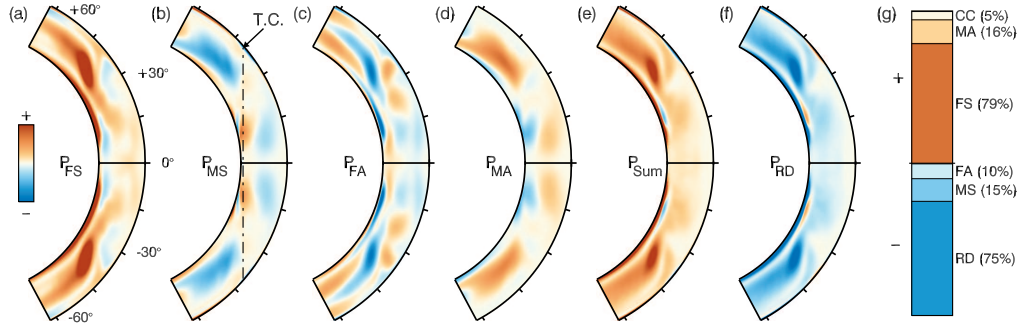


Figure 7.: Generation of mean poloidal magnetic energy ( $P_{ME}$ ) in  $K3S$ . The dominant production/destruction terms are shown, namely (a) fluctuating shear ( $P_{FS}$ ), (b) mean shear ( $P_{MS}$ ), (c) fluctuating advection ( $P_{FA}$ ), (d) mean advection ( $P_{MA}$ ) and (e) the sum  $P_{MS} + P_{FS} + P_{MA} + P_{FA} + P_{CC}$ , with (f) the resistive diffusion of field ( $P_{RD}$ ). The mean generation terms shown contribute to the  $P_{ME}$  when positive (red), and destroy it if negative (blue). (g) The relative contribution of each term, with those in red adding to the volume- and time-averaged poloidal energy generation and those in blue dissipating energy.

production due to the compressibility of the downflows, which can be seen from the form of  $T_{CC}$ , plays a weak but supporting role. In keeping with the dominance of the  $\Omega$  effect ( $T_{MS}$  above), the toroidal magnetic energy generation is greatest at latitudes where the latitudinal gradients in the differential rotation are at their largest. This maximum occurs at latitudes outside the tangent cylinder in a roughly  $15^\circ$  swath, though there is also generation of toroidal field at higher latitudes just inside the tangent cylinder. The resistive dissipation and fluctuating advection of field act in tandem to destroy toroidal field. Given the spatial distribution of  $T_{FA}$  in Figure 6b, the action of the fluctuating advection could be considered as part of an  $\alpha$ -effect with the small-scale flows tearing at the large-scale wreaths, transferring energy from the toroidal to the poloidal magnetic fields.

The relative contributions of each term have been measured by integrating them over time and space  $\langle T_i \rangle = \int T_i dV$ , where  $i$  is any of the terms in Equation (1). This allows the net action of a given term to be assessed, indicating whether it on average is productive or destructive of toroidal magnetic energy. As indicated in Figure 6(f), the bulk of the production is accomplished by  $T_{MS}$ , being about 92% of the total. The remaining 8% of the mean production is due mostly to the compressive motions of the downflows ( $T_{CC}$ ). In contrast, the averaged  $T_{RD}$ ,  $T_{FA}$ ,  $T_{MA}$ , and  $T_{FS}$  processes act in concert to dissipate magnetic energy, with  $T_{RD}$  responsible for 68% of the dissipation and  $T_{FA}$  24%.

The mechanisms generating the poloidal fields and its associated magnetic energy  $P_{ME}$  are given in Equation (2). In Figure 7, the temporal and longitudinal averages of the generation terms with the largest average contributions are shown. The average is again carried out over 80 years. Figure 7(g) shows that in the spatially integrated sense and unlike in the toroidal energy generation, the fluctuating shear  $P_{FS}$  is the dominant contributor to the production of poloidal field, generating on average 79% of the poloidal energy, while the resistive diffusion  $P_{RD}$  again is the largest dissipator, destroying 75% of it. However, other processes contribute to the generation of poloidal field as well. The production

of poloidal field arises through the joint action of the fluctuating shear  $P_{FS}$  and mean advection  $P_{MA}$ , whereas the dissipation of poloidal magnetic energy arises from the combination of resistive diffusion  $P_{RD}$  and mean shear  $P_{MS}$ . The bulk of the production occurs near the lower boundary and inside the tangent cylinder, being associated with the fluctuating velocities and magnetic fields of the more isotropic convective cells at higher latitudes. The generation of poloidal field has two primary balances: the first is between production through the fluctuating shear and resistive decay; the second is between the mean shear and the mean advection. The overall balances of magnetic energy generation are subtle given the spatial separation between the primary regions of toroidal and poloidal field generation, with poloidal field being built near the base of the convection zone and at higher latitudes and the toroidal field being produced at low latitudes in the upper convection zone.

## 7. Equatorward Dynamo Wave Propagation

As with ASH and EULAG, simulations in spherical segments that employ the Pencil code have also obtained regular cyclic magnetic behavior. Some of these polarity reversing solutions exhibited equatorward propagating magnetic features (Käpylä et al., 2012, 2013), magnetic flux ejection (Warnecke et al., 2012), and 33-year magnetic polarity cycles (Warnecke, 2013). Currently, however, the mechanism for the equatorward propagation of the magnetic structures in those simulations remains unclear. Perhaps the mechanism is similar to that seen here.

The equatorward propagation of magnetic features observed in K3S, as in Figures 4(c) and 5(a), arises through two mechanisms. The first process is the nonlinear feedback of the Lorentz force that acts to quench the differential rotation, disrupting the convective patterns and the shear-sustaining Reynolds stresses they possess. Since the latitudinal shear serves to build and maintain the magnetic wreaths, the latitude of peak magnetic energy corresponds to that of the greatest shear. So the region with the largest magnetic potential energy in the form of latitudinal shear moves progressively closer to the equator as the Lorentz forces of the wreaths locally weaken the shear. Such a mechanism explains the periodic modifications of the differential rotation seen in Figure 2(c). However, it does not explain how this propagation is initiated and sustained, as one might instead expect an equilibrium to be established with the magnetic energy generation balancing the production of shear and which is further moderated by cross-equatorially magnetic flux cancellation as the distance between the wreaths declines.

There are two possibilities for the second mechanism that promotes the equatorward propagation of toroidal magnetic field structures. If the dynamo action in this case may be considered as a dynamo wave, the velocity of the dynamo wave propagation is sensitive to the gradients in the angular velocity and the kinetic helicity in the context of an  $\alpha\Omega$  dynamo (e.g., Parker, 1955; Yoshimura, 1975). This dynamo-wave velocity is given as  $\mathbf{S} = -\lambda\alpha\hat{\phi} \times \nabla\Omega$ , where  $\lambda = r \sin\theta$ . The basic  $\alpha$ -effect has  $\alpha = -\tau_o\langle\mathbf{v} \cdot \boldsymbol{\omega}\rangle/3$ , and so depends on the convective overturning time  $\tau_o$  and the kinetic helicity. These quantities are shown in Figure 8 with time-latitude, time-radius, and time-averaged plots over the average cycle. This simple analysis indicates that near and poleward of the edge of the low-latitude wreaths the sign of the Parker-Yoshimura mechanism is correct to push the dy-

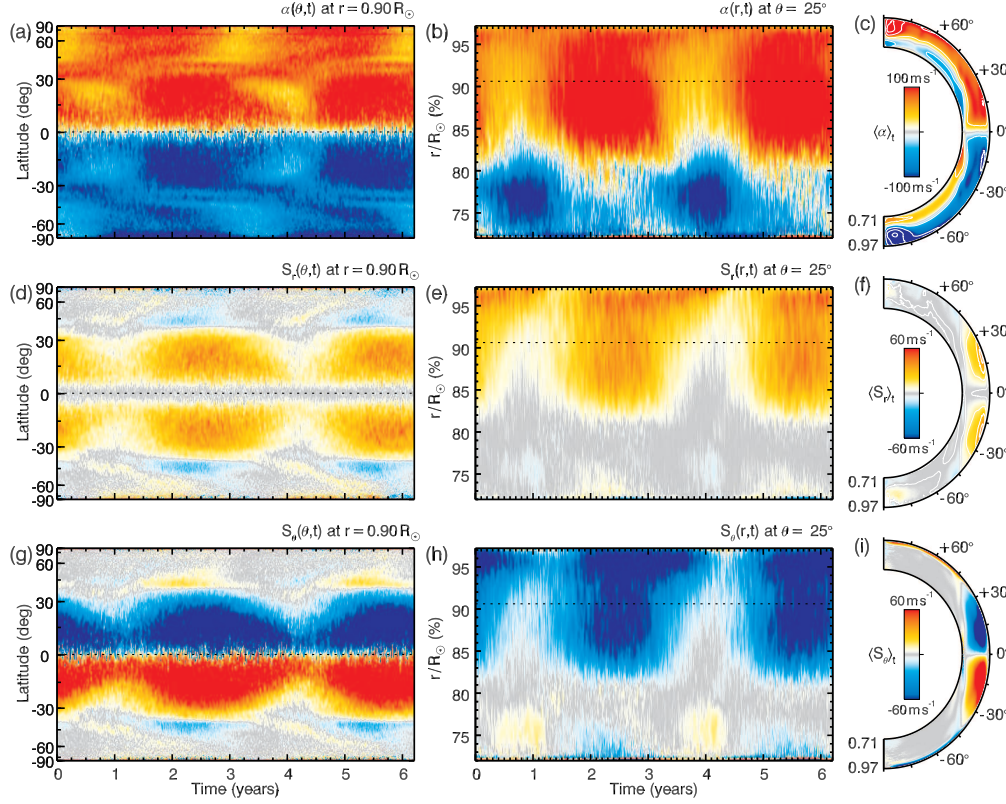


Figure 8.: A mean-field interpretation of the  $K3S$  dynamo over the average cycle. The isotropic  $\alpha$ -effect arising from the kinetic helicity is shown (a) with latitude and time, (b) with radius and time, and (c) averaged over the cycle. The radial velocity  $S_r$  and latitudinal velocity  $S_\theta$  of the dynamo wave propagation within the context of the Parker-Yoshimura mechanism are exhibited in (d-i). (d) A radial cut at  $0.90 R_\odot$  through the radial propagation  $S_r$  of the dynamo wave, outward propagation is in red and downward in blue. (e) A latitudinal cut through  $S_r$ , colors as in (d) and the dotted line indicates the depth of the radial cut in (d). (f)  $S_r$  averaged over the cycle and shown in the meridional plane. Figures (g-i) are as in (d-f), but for  $S_\theta$ , with the latitudinal propagation is equatorward at latitudes above  $30^\circ$  and largely poleward at lower latitudes (blue in the northern hemisphere and red in the south).

namo wave toward the equator, but the effect is marginal elsewhere. The second possibility is that the spatial and temporal offsets between the fluctuating EMF and the mean-shear production of toroidal field leads to a nonlinear inducement to move equatorward. This mechanism relies on the concurrent movement of the turbulent production of the poloidal field that continues to destroy gradients in angular velocity through the production of toroidal magnetic through the action of the differential rotation on the renewed low-latitude poloidal field.

## 8. Conclusions

The ASH simulation K3S presented here is the first to self-consistently exhibit four prominent aspects of solar magnetism: regular magnetic energy cycles during which the magnetic polarity reverses, akin to the sunspot cycle; magnetic polarity cycles with a regular period of 6.2 years, where the orientation of the dipole moment returns to that of the initial condition; the equatorward migration of toroidal field structures during these cycles; and an interval of magnetic quiescence after which the previous polarity cycle is recovered. Furthermore, this simulation may capture some aspects of the influence of a layer of near-surface shear, with a weak negative gradient in  $\langle\Omega\rangle$  within the upper 10% of the computation domain (3% by solar radius). The magnetic energy cycles with the time scale  $\tau_C/2$  arise through the nonlinear interaction of the differential rotation and the Lorentz force. The magnetic fields further quench the differential rotation by impacting the convective angular momentum transport during the reversal. Despite the nonlinearity of the case, there is an eligible influence of a dynamo wave in the fluctuating production of poloidal magnetic field linked to the shear-produced toroidal field. The possible mechanisms producing the equatorward propagation of the toroidal fields have been examined, with the nonlinear dynamo wave character of the solution and the nonlocal interaction of the turbulent EMF and the mean-shear production of toroidal field all playing a role. However, the dominant mechanism behind the equatorward propagation is the nonlinear feedback of the Lorentz force on the differential rotation. This simulation has also exhibited grand minima, similar to a Maunder minimum. Indeed, there is an interval covering 20% of the cycles during which the polarity does not reverse and the magnetic energy is substantially reduced. Hence, some of the features of the dynamo active within the Sun's interior may have been captured in this global-scale ASH simulation.

*Acknowledgements.* A singular thanks is due to Nicholas Featherstone for his effort in greatly improving the computational efficiency and scaling of the ASH code, without which this work would not have been possible. The authors also thank Brad Hindman, Mark Rast, Matthias Rempel, and Regner Trampedach for useful conversations. The author thanks the NCAR advanced study program for their continuing support, as well as the support provided by NASA through the Heliophysics Theory Program grant NNX11AJ36G. The computations were primarily carried out on Pleiades at NASA Ames with SMD grants g26133 and s0943, and also used XSEDE resources for analysis. This work also utilized the Janus supercomputer.

## References

- Augustson, K. C., Brun, A. S., & Toomre, J. 2013, *ApJ*, 777, 153
- Brown, B. P., Browning, M. K., Brun, A. S., Miesch, M. S., & Toomre, J. 2010, *ApJ*, 711, 424
- Brown, B. P., Miesch, M. S., Browning, M. K., Brun, A. S., & Toomre, J. 2011, *ApJ*, 731, 69
- Browning, M. K., Miesch, M. S., Brun, A. S., & Toomre, J. 2006, *ApJ*, 648, L157
- Brun, A. S., Miesch, M. S., & Toomre, J. 2004, *ApJ*, 614, 1073



- Charbonneau, P. 2013, *Nature*, 493, 613
- Clune, T. L., Elliott, J. R., Miesch, M. S., Toomre, J., & Glatzmaier, G. A. 1999, *Para. Comp.*, 25, 361
- DeRosa, M. L., Brun, A. S., & Hoeksema, J. T. 2012, *ApJ*, 757, 96
- Fan, Y., Featherstone, N., & Fang, F. 2013, ArXiv e-prints
- Ghizaru, M., Charbonneau, P., & Smolarkiewicz, P. K. 2010, *ApJ*, 715, L133
- Gilman, P. A. 1983, *ApJS*, 53, 243
- Glatzmaier, G. A. 1985, *ApJ*, 291, 300
- Hathaway, D. H. 2010, *Living Reviews in Solar Physics*, 7, 1
- Käpylä, P. J., Mantere, M. J., & Brandenburg, A. 2012, *ApJ*, 755, L22
- Käpylä, P. J., Mantere, M. J., Cole, E., Warnecke, J., & Brandenburg, A. 2013, ArXiv e-prints
- Malkus, W. V. R., & Proctor, M. R. E. 1975, *Journal of Fluid Mechanics*, 67, 417
- Miesch, M. S., Elliott, J. R., Toomre, J., et al. 2000, *ApJ*, 532, 593
- Nelson, N. J., Brown, B. P., Brun, A. S., Miesch, M. S., & Toomre, J. 2013, *ApJ*, 762, 73
- Parker, E. N. 1955, *ApJ*, 122, 293
- . 1977, *ARA&A*, 15, 45
- . 1987, *ApJ*, 312, 868
- Racine, É., Charbonneau, P., Ghizaru, M., Bouchat, A., & Smolarkiewicz, P. K. 2011, *ApJ*, 735, 46
- Rempel, M., Schüssler, M., & Knölker, M. 2009, *ApJ*, 691, 640
- Steenbeck, M., & Krause, F. 1969, *Astronomische Nachrichten*, 291, 49
- Tobias, S. M. 1997, *A&A*, 322, 1007
- Warnecke, J. 2013, PhD thesis, University of Stockholm
- Warnecke, J., Käpylä, P. J., Mantere, M. J., & Brandenburg, A. 2012, *Solar Phys.*, 280, 299
- Weiss, N. O., Cattaneo, F., & Jones, C. A. 1984, *Geophysical and Astrophysical Fluid Dynamics*, 30, 305
- Yoshimura, H. 1975, *ApJ*, 201, 740